Journal of Solid State Chemistry 315 (2022) 123474

Contents lists available at ScienceDirect

Journal of Solid State Chemistry

journal homepage: www.elsevier.com/locate/jssc

Thermally dynamic examination of local order in nanocrystalline hydroxyapatite

Emily L. Arnold [a,*], Sarah Gosling [a], Samantha K. Davies [a], Hannah L. Cross [b], Paul Evans [c], Dean S. Keeble [d], Charlene Greenwood [b], Keith D. Rogers [a]

[a] Cranfield Forensic Institute, Cranfield University, Shrivenham, Wiltshire, SN6 8LA, UK
[b] School of Chemical and Physical Sciences, Keele University, Keele, Staffordshire, ST5 5BJ, UK
[c] Imaging Science Group, Nottingham Trent University, Rosalind Franklin Building, Nottingham, NG11 8NS, UK
[d] Diamond Light Source Ltd, Diamond House, Harwell Campus, Didcot, Oxfordshire, OX11 0DE, UK

ARTICLE INFO

Keywords:
Hydroxyapatite
Powder X-ray diffraction (PXRD)
Total scattering
Pair distribution function (PDF)

ABSTRACT

The main mineral component of bone is hydroxyapatite, a commonly nanocrystalline material which presents many challenges for those trying to characterize it. Here, local structure is analyzed using X-ray total scattering for synthetic samples, to enable a better understanding of the nanocrystalline nature of hydroxyapatite. Two samples were measured dynamically during heat treatment from 25 °C to 800 °C, and were analyzed using small box modelling. Analysis of sequential measurements when dwelling at key temperatures showed a significant relationship between time and temperature, indicating a process occurring more slowly than thermal expansion. This indicates a decrease in B-type CO_3^{2-} substitution between 550 °C and 575 °C and an increase in A-type CO_3^{2-} substitution above 750 °C. A greater understanding of local, intermediate, and long-range order of this complex biomineral during heat treatment can be of interest in several sectors, such as in forensic, biomedical and clinical settings for the study of implant coatings and bone diseases including osteoporosis and osteoarthritis.

1. Introduction

Bone is primarily comprised of a calcium phosphate crystallographic phase often described as hydroxyapatite (HA), seen in Fig. 1 [1]. Many ionic substitutions are frequently present in biogenic HA in contrast to synthetic HA where fewer substitutions need to be considered. Perhaps the most biologically significant substitution is carbonate (CO_3^{2-}) which accounts for between 5 wt % and 9 wt% of biological HA [2]. Carbonate substitution has been seen to affect crystallite properties such as solubility, morphology, and size [3–6]. Composition of co-substituted A-type and B-type carbonated HA is described by equation (1):

$$Ca_{(10-x)}(PO_4)_{(6-2x)}(CO_3)_{2x}(OH)_{(2-y)}(CO_3)_y \quad \text{Equation 1}$$

where *2x* represents the level of B-type CO_3^{2-} substitution and *y* represents the amount of A-type CO_3^{2-} substitution. A-type CO_3^{2-} substitution occupies the *c*-axis channel while the B-type substitution occupies the tetrahedral site, often on one face of the PO_4^{3-} [7–9].

The structural modifications of synthetic and biogenic HA during heat treatment are important for several sectors including biomedical research, forensic science, and archaeology [10–14]. While the effects of heat treatment on bone are heavily researched, the underlying chemical processes are not well understood. Due to the multitude of factors that can impact the result of heat treatment on the bone, many studies attempt to undertake thorough and reproducible serials of controlled heat treatment of biogenic, geological and synthetic HA [9,15–19], though few examine these differences dynamically using X-ray diffraction (XRD) [9,18,20].

During heat treatment several characteristics are commonly observed. Reversible loss of unbound or surface H_2O is observed from room temperature to 200 °C [9,21]. Irreversible loss of lattice-bound water (commonly thought to occupy the ion channel) occurs from 200 °C to 400 °C [9,20–22]. However, there are conflicting accounts concerning structural changes between 400 °C and 700 °C. While Fourier transform infrared spectroscopy (FTIR) analysis of dental enamel at room temperature has shown a simultaneous decrease in B-type carbonate and an increase in A-type carbonate when heated between 350 °C and 700 °C [23], dynamic XRD analysis has indicated a relatively rapid change in lattice parameters between 600 °C and 700 °C (dependent on HA source) which corresponds to an increase in A-type or a decrease in B-type

* Corresponding author.
E-mail address: e.l.arnold@cranfield.ac.uk (E.L. Arnold).

https://doi.org/10.1016/j.jssc.2022.123474
Received 13 June 2022; Received in revised form 25 July 2022; Accepted 2 August 2022
Available online 10 August 2022

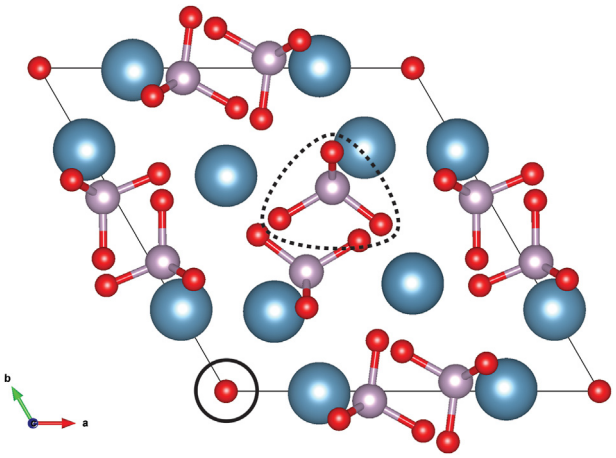

Fig. 1. Hydroxyapatite unit cell: calcium is shown in blue, oxygen in red and phosphorous in purple. The location of A-type CO_3^{2-} is shown with the solid line, and B-type CO_3^{2-} is shown with the dashed line.

carbonate [20]. Unfortunately, due to limitations of analytical techniques (either XRD due to the nanocrystalline nature of most biogenic HA or FTIR due to overlapping absorption bands) it is difficult to reliably determine carbonate site distribution using these methods. Currently it is unclear whether A-type carbonate increases during heating, or if this 'transformation' from B-type to A-type sites only occurs during cooling, a process which is not well-understood [20]. Above 600 °C recrystallisation of HA begins, resulting in rapid crystallite growth [20]. Both biogenic and synthetic HA are known to produce multiple phases during heat treatment due to thermal decomposition of HA [10,20,24] at temperatures above 710 °C–900 °C, depending on HA source (e.g. synthetic, bone, tooth, etc.).

Several studies, perhaps most notably LeGeros et al. [25,26], have recorded the consequence of both A-type and B-type CO_3^{2-} substitution on HA lattice parameters [27–29]. The limitation of most of these studies is that synthetic samples are synthesized at elevated temperatures (in excess of 80 °C) in an effort to exclude lattice-bound water. In other synthetic samples synthesized at low temperatures, as well as biogenic samples, this lattice-bound water and additional inclusions can further confound interpretation of lattice parameters [30,31].

Currently most carbonate site determination is done *via* FTIR, using either the $\nu_2CO_3^{2-}$ absorption band or the $\nu_3CO_3^{2-}$ absorption band, though both present their own problems, particularly in biogenic samples [32–36].

In this study, two synthetic HA samples were subjected to heat treatment during simultaneous X-ray pair distribution function (PDF) and XRD data collection that was subsequently analyzed using a small box modelling procedure. This work is the first to examine the local order of nanocrystalline synthetic hydroxyapatite dynamically over a range of temperatures from 25 °C to 800 °C. The unique examination of lattice parameters over time at each temperature allows for better analysis of the processes which occur. This study is also the first examination of unit cell structure dynamically during heating, not just the lattice parameters. It is expected that examination of local order during dynamic heat treatment will be beneficial to a range of disciplines such as clinical and biomedical research, as well as validate previous dynamic and static observations.

2. Experimental section

2.1. Materials

Two synthetic apatites were used in this study with 4.68 wt% CO_3^{2-} (CHA-1) and 6.54 wt% CO_3^{2-} (CHA-2). Both samples were synthesized using the method described previously in Arnold et al. [37], and adapted from the method described in Merry et al. [38]. Samples were homogenized mechanically using an agate mortar and pestle and the resulting powders were sieved using a 106 μm mesh. Only the sieved powder was used to reduce preferred orientation effects and improve particle statistics. Samples were characterized using conventional XRD, total scattering and attenuated total reflectance (ATR) FTIR as described in Arnold et al. [37]. Each method will be described in brief below.

2.2. XRD

Laboratory based XRD data were collected using a PANalytical X'Pert PRO Multi-Purpose Diffractometer with Cu Kα radiation source. A PIXcel strip detector was used to collect data from 10° to 80° 2θ. Topas (Bruker, Version 4.1) was used to fit diffraction profiles using a full profile refinement procedure. Lattice parameters (LPs) were calculated from all samples after correction using internal spiking with a silicon standard (NIST SRM 640c).

2.3. FTIR

FTIR was used to estimate carbonate levels to provide relative carbonate amount. Spectra were collected using a Bruker Alpha with a diamond ATR crystal, and a scan range from 4000 cm^{-1} to 400 cm^{-1}, 64 averaged scans and 4 cm^{-1} resolution. All FTIR spectra were analyzed using Spectrum (PerkinElmer). Area was measured for the $\nu_1\nu_3PO_4^{3-}$ peak and $\nu_2CO_3^{2-}$ peak after background subtraction. Spectra were deconvoluted until peak centers were apparent near A-type, B-type and labile CO_3^{2-} sub-bands (878 cm^{-1}, 873 cm^{-1} and 866 cm^{-1}). Three Voigt peaks with peak centers fixed at values determined *via* deconvolution were fit using PeakFit4 (Sigmaplot), once the spectra was limited to 910 cm^{-1} to 840 cm^{-1} and baseline corrected. A CO_3^{2-} concentration calibration curve described previously [39] was used to determine CO_3^{2-} concentration using the ratio of $\nu_2CO_3^{2-}$: $\nu_1\nu_3PO_4^{3-}$ peak areas.

2.4. Total scattering

Experimental PDFs were acquired from I15-1 beamline at Diamond Light Source, using 76.7 keV radiation (λ = 0.161669 Å). Two data sets were collected simultaneously, one used for total scattering analysis (Q-range = 0 $Å^{-1}$ - 38.86 $Å^{-1}$) and the other used for fitting of Bragg peaks (Q-range = 4.05 $Å^{-1}$ – 8.12 $Å^{-1}$) using a full profile refinement procedure similar to that used for laboratory XRD. DAWN [40] was used to integrate the 2D area data to 1D data. Data was collected at 25 °C, 100 °C, 200 °C, 300 °C, 325 °C, 350 °C, 400 °C, 450 °C, 500 °C, 550 °C, 575 °C, 600 °C, every 10 °C–700 °C, 750 °C and 800 °C. The heating rate between temperatures was 10 °C min^{-1}, and data was collected at each stated temperature for 10 min. Decreased steps between temperatures were chosen at key intervals based on literature [10,20]. A background (consisting of an empty capillary) was measured at room temperature, 400 °C, 600 °C, 650 °C and 700 °C. Details of which background collection was subtracted from each temperature can be seen in Supplementary Table S1.

The CHA-1 was measured with one frame per temperature, producing a total of 24 frames covering 24 temperatures. CHA-2 was measured with 10 frames per temperature, producing a total of 230 frames. Due to unanticipated shut-down of the beam, 19 of these frames held no useable data, leaving a total of 211 frames which were used for further analysis, covering 22 temperatures in addition to the single 10 min frame collected at room temperature.

GudrunX [41] was used to process PDFs with a Q_{min} = 0.5 $Å^{-1}$ and Q_{max} = 25.6 $Å^{-1}$. Sample composition was calculated using the CO_3^{2-} concentration for all samples; Equation (1) was used to calculate composition assuming no additional substitutions. Composition and Si-spiked lattice parameters were used to calculate sample density. For CHA-2, all frames from each temperature were used to calculate one PDF to improve Q_{max}.

Topas6 Academic [42,43] was used to analyze PDF data. A silicon

standard (NIST SRM 640c) was refined to determine instrumental damping. Due to the typical platy morphology of nanocrystalline HA, a nano-sheet damping profile was also applied during processing, with refinement of the nano-sheet thickness according to Kodama [44] and given below:

$$G_{sheet}(r) = \begin{cases} \dfrac{(t - r/2)}{t} & if\ r \le t \\ \dfrac{t}{2r} & if\ r > t \end{cases} \qquad \text{Equation 2}$$

where t is the thickness of the nano-sheet and r is the radius of the PDF.

A P1 space group expanded from the structure given in Kay et al. [45] was used for small box modelling, with symmetry constraints manually imposed during fitting. Atomic coordinates describing the asymmetric unit were refined and multiplicities were expanded using the Wyckoff positions of $P6_3/m$, for all atomic species apart from the oxygen within the ion channel (in the *4e* Wyckoff position). Two positions were chosen [(0,0,*z*) and (0,0,*z*+½)] to be fully occupied. This method was chosen to eliminate false peaks within the calculated PDF which arose from *4e* sites within the usual $P6_3/m$ space group which are partially occupied. The assumption that these sites are all simultaneously partially occupied produces such false peaks, as some combination of sites present a non-physical structure. Each PO_4^{3-} was modelled as a rigid body with five atoms: P, O1, O2, O3a and O3b. All rigid body parameters are shown in Fig. 2. A spherical function was applied to determine temperature factor in order to model correlated motion at a low radius [46]. The spherical function is dependent on three parameters as given in Equation (3) and seen in Fig. S1.

$$B = \begin{cases} beqlo + (beqhi - beqlo)\left[1 - \dfrac{\pi r^2\left(\frac{1}{4}\left(\frac{r}{beqradius}\right)^3 - 3\frac{r}{beqradius} + 4\right)}{4\pi r^2}\right], & r < 2{*}beqradius \\ beqhi, & r \ge 2{*}beqradius \end{cases} \qquad \text{Equation 3}$$

This method resulted in a total of 40 refined parameters. The same initial values were used for each refinement, and the refinement was allowed to continue until the model converged.

3. Results

Two carbonated HA samples were analyzed over a temperature range from 25 °C to 800 °C. FTIR spectra for unheated samples are given in Fig. S2. Selected exemplary small box refinements can be seen in Fig. S3. Differences can be easily observed in data from both detectors, though most notably in the low 2θ region (where Q < 1 $Å^{-1}$) which decreases significantly with increasing temperature. This implies a reduction in small-angle scattering due to a change in nano-scale crystallite size. Additionally, sharpening of peaks can be observed with a slight shift of peaks to a lower angle (illustrated in Fig. 3a). A systematic shift is expected when examining materials at increasing temperatures due to expansion of the lattice. When examining the PDFs in Fig. 3b, this systematic shift is readily apparent.

When considering results of small box modelling, the variation in sheet thickness (the smallest dimension of the crystallite, refined using Equation (2)) with respect to temperature should be noted (seen in Fig. 4) as it can be compared to dynamic studies from literature. While differences were observed between the two samples analyzed at low temperatures, above 550 °C sheet thickness for both samples steadily increased.

3.1. Lattice parameters

Changes to the lattice parameters are shown in Fig. 5a and b. Of particular note is the region from ~500 °C to 700 °C, which is seen in greater detail in Fig. 5c and d and shows values of *a* and *c* for each frame of CHA-2. While changes within the LPs are subtle, there is a rapid increase in *a* between 575 °C and 600 °C followed by a more subtle decrease (relative to expected thermal expansion) from 600 °C to 620 °C. Concomitantly, a plateau is seen in the *c* axis over the same temperature range (particularly visible in Fig. 5c and d).

To further examine these changes, lattice parameters for CHA-2 were plotted and grouped according to the time in Fig. 5c and d. Using this approach, significantly greater variation is observed in the *c* axis between frames for each temperature interrogated relative to overall change in LP. A clear trend can be seen in temperatures between 550 °C and 660 °C, where *c* is highest for the first frame and gradually decreases as the frame number increases (the dwell time at that particular temperature increases).

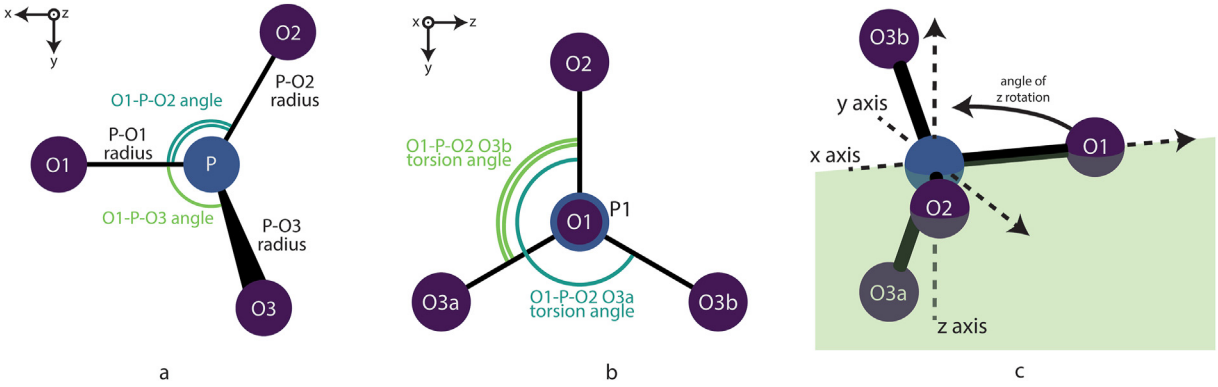

Fig. 2. Rigid body parameters, *a)* showing the radii P–O1, P–O2 and P–O3 and angles O1–P–O2 and O1–P–O3. *b)* showing the torque angles O3a and O3b with the *xy* plane (bisecting P, O1 and O2). *c)* rotation about the *z* axis where P, O1 and O2 are now positioned on the mirror plane.

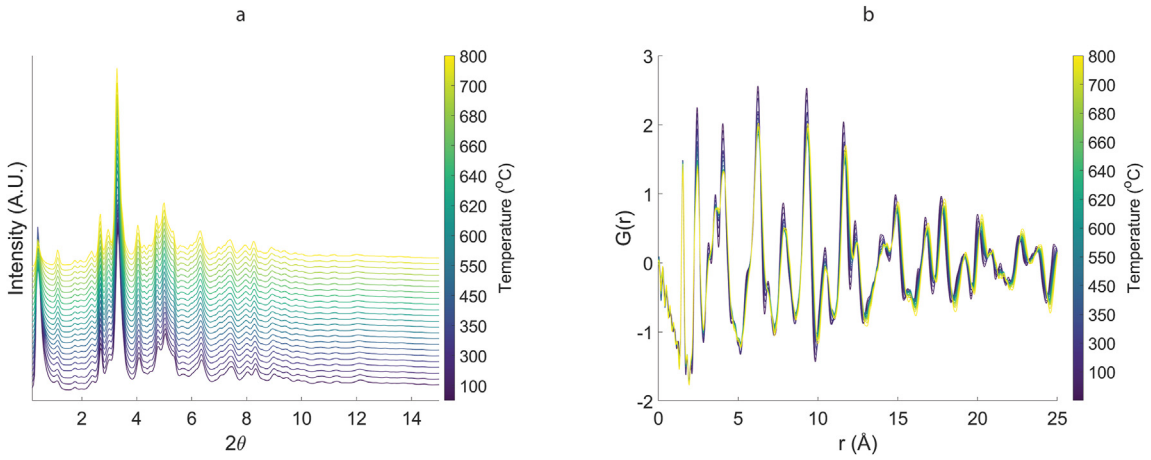

Fig. 3. *a)* Diffractograms and *b)* PDFs from detector 2 for CHA-1.

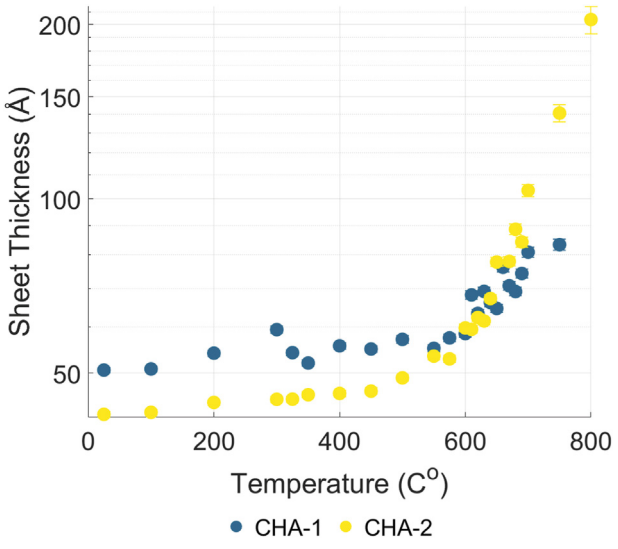

Fig. 4. Sheet thickness (*t*) correlated to temperature for both samples used in dynamic studies. Error bars represent estimated standard deviation.

To further examine these relationships, LPs were examined with time of measurement (Fig. 6). For each temperature group, a linear regression was performed to determine which LP changes were significantly correlated with time (rate of change (Å min^{-1}) is given in Table S2). Clear outliers (such as the last frame collected at 100 °C and the last frame collected at 400 °C) were removed for both *a* and *c* before linear regression. Five temperature sets saw a significant trend with time ($p < 0.05$): 550 °C, 575 °C, 700 °C, 750 °C and 800 °C. For four of these five sets, *a* significantly increases while *c* significantly decreases, while at 700 °C both *a* and *c* decrease significantly.

This trend of decreasing LPs with dwell time indicates that there is at least one process (such as increase or evacuation of CO_3^{2-}) which is occurring more slowly than both the ramp rate of heating between measurements (10 °C min^{-1}) and the measurement time (1 min/frame).

3.2. Unit cell contents

P1 stoichiometric structures were used to refine dynamic measurements of CHA-1 and CHA-2. Fractional coordinates, rigid body parameters and occupancies of atomic species were further analyzed below.

Fractional coordinates of the $P6_3/m$ asymmetric unit were plotted against temperature in Fig. S4. Rigid body parameters were plotted against temperature in Fig. S5. Occupancy of atomic species were plotted against temperature in Fig. 7 and Fig. S6.

It should be noted here that OH^- was not observed in FTIR spectra (absorption bands near 3560 cm^{-1} and 630 cm^{-1}) for either CHA-1 or CHA-2. However, an H–O–H absorption band arising from water is apparent in FTIR spectra of both samples [23,47]. It is proposed that the irregular refinement of the O(H) occupancy below ~300 °C corresponds to lattice-bound water occupying the ion channel.

It is expected that the bond angles may change, as well as the positioning of the molecule within the unit cell in reaction to a potentially changing environment around the rigid body. It would be anticipated if the amount of B-type CO_3^{2-} decreased then this would be reflected in the rigid body through changes to bond lengths (at least one or more would be expected to increase) and bond angles (a more tetrahedral arrangement would be expected, compared to a more planar arrangement which would suggest a higher substitution of B-type CO_3^{2-}) [9].

When considering fractional coordinates (seen in Fig. S4), there are no clear changes of P *x* and P *y*. Ca1 *z* increases by ~0.3% from 25 °C to 300 °C, and then remains constant. However, clear changes can be seen in values for Ca2 *x* and Ca2 *y*. While Ca2 *x* does not change significantly from 25 °C to 200 °C, its value decreases significantly from 300 °C to ~575 °C, and subsequently remains constant above 600 °C. In contrast, Ca2 *y* increases significantly from 25 °C to 300 °C, remains constant from ~300 °C to 575 °C, and then decreases (more notably for CHA-2). When O(H) *z* is considered, there is no substantial change until 300 °C. From 300 °C to 575 °C O(H) *z* remains constant and above 575 °C both samples increase.

When examining rigid body parameters (seen in Fig. S5), few relationships are present, though it should be noted all three P–O radii slightly increase.

Several interesting trends are observed when the occupancies of atomic species are considered (shown in Fig. 7 and Fig. S6). P occupancy begins near 0.80 and 0.84 for CHA-2 and CHA-1 respectively. The occupancy of P steadily increases to ~0.9, the level of other low temperature synthetic samples (with relatively small CO_3^{2-} concentration) at room temperature. O1 site occupancy begins ~0.875 and increases to ~0.925 at 300 °C then varies greatly from 300 °C to 800 °C. Similarly, O3 site occupancy varies over the entire temperature range examined. In contrast, O2 site occupancy increases from 25 °C to 400 °C, remains constant until around 580 °C–600 °C, then decreases sharply above 600 °C. Occupancy of Ca1 increases slightly to 300 °C, decreases to 600 °C, then rapidly increases above 600 °C. In contrast, Ca2 site occupancy increases to 200 °C, stays constant until ~600 °C, then increases sharply. It should be noted that while the occupancy of Ca2 increases to just above 1 for both samples, occupancy of Ca1 increases to ~0.9. The <1 occupancy of Ca1 may be a consequence of Na + substitution, which would be

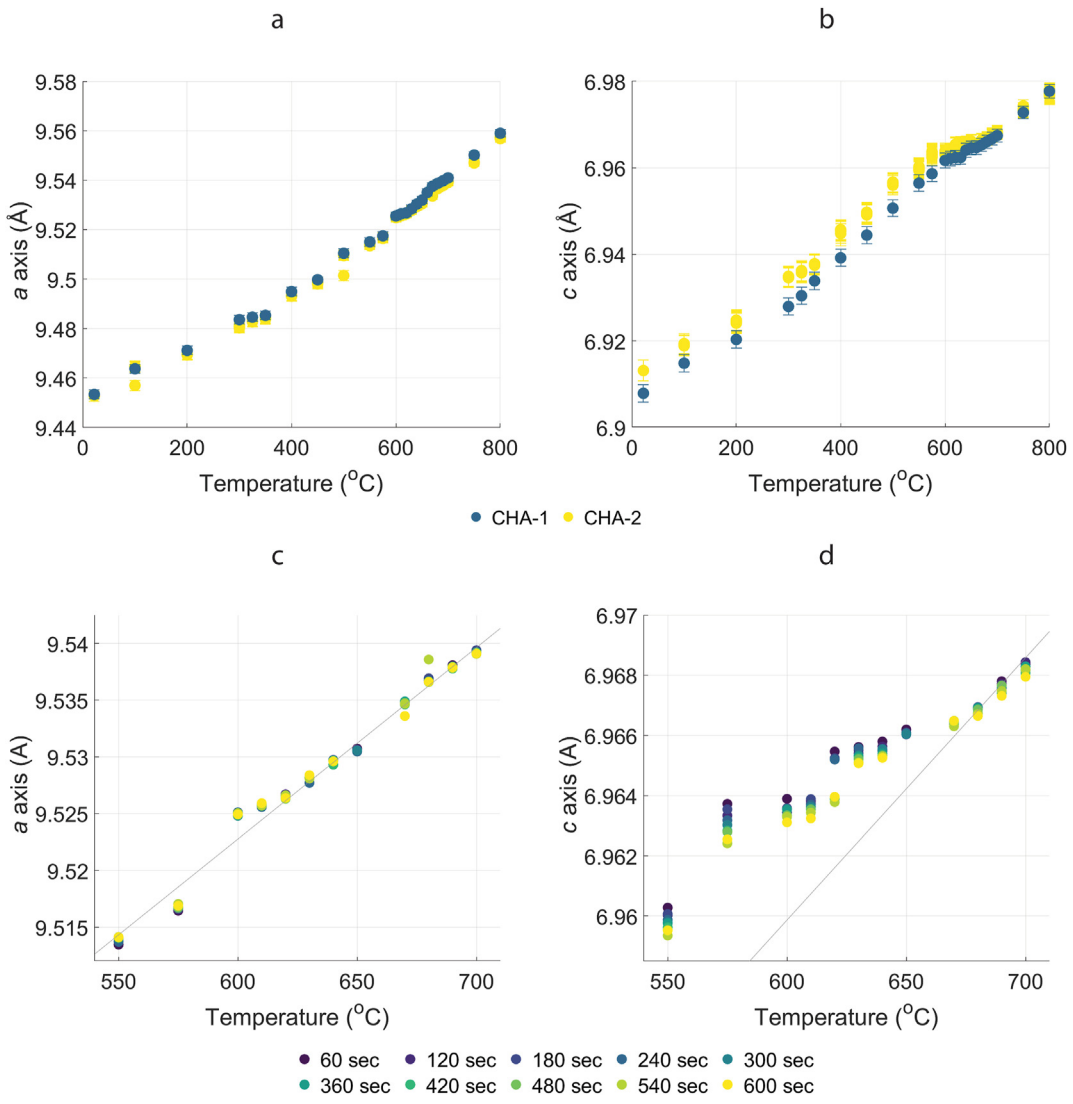

Fig. 5. Lattice parameters for dynamic measurements. *a)* and *b)* show *a* and *c* lattice parameters both CHA-1 and CHA-2 across all temperatures. *c)* and *d)* show a and c lattice parameters for CHA-2 for each frame, from 500 °C to 700 °C. Lines which represent thermal expansion above 650 °C have been added to provide clarity. Error bars represent estimated standard deviation in *a)* and *b)*; for *c)* and *d)* error bars are omitted for clarity.

expected from the synthesis method used [38,48]. Occupancy of O(H) increases to ~350 °C, then decreases to ~600 °C.

Using the occupancies refined during fitting, the calcium:phosphorous ratio (Ca:P) was calculated for all temperatures and is shown in Fig. S7. While Ca:P initial value is 1.85 for CHA-2 and 1.8 for CHA-1, it decreases for both samples to ~1.75 at 800 °C.

beq parameters were also considered during analysis (seen in Fig. S8). As temperature increases, *beq* radius decreases. Interestingly, *beqlo* for both P, O1, O2 and O3 are consistently refined to the minimum allowable value (0.001 Å^2), as is O(H). While *beqhi* values for all atom species begin increasing with increasing temperature, their patterns diverge above 300 °C. *beqhi* P steadily increases until between 500 °C and 575 °C, where both decrease until about 630 °C. *beqhi* O1, O2 and O3 all increase steadily over the temperature range measured. Interestingly, *beqhi* O2 seems to peak around 575 °C–600 °C, and decreases slightly above 600 °C. Perhaps of most interest here is *beqhi* of O(H), which increases until around 300 °C, then sharply decreases above 300 °C.

4. Discussion

A previous study of synthetic HA using PDF analysis at room temperature showed the dependence of several structural factors on CO_3^{2-} concentration [39]. The few studies that have examined heated HA dynamically using XRD, such as Greenwood et al. [20] and Ivanova et al. [9] showed key structural changes in the lattice parameters at temperatures consistent with those of our study.

Consideration of sheet thickness shows that recrystallisation of the mineral commences between 575 °C and 600 °C. Whilst this range is similar to previous synthetic studies, recrystallisation begins at slightly lower temperatures to those seen in biological samples [18,20]. This is potentially due to the presence of collagen and other stabilizing organic molecules. Greenwood et al. observed differences in the onset (and rate) of recrystallisation dependent on species with varying quantities of collagen, and as such variation between synthetic and biogenic samples would also be expected. The likely cause in the difference of recrystallisation seen here in Fig. 4 is the different CO_3^{2-} substitution. It is readily apparent that the sheet thickness is higher in CHA-1, with a lower CO_3^{2-} concentration, and that CHA-2, with a higher CO_3^{2-} concentration, undergoes more aggressive recrystallisation. As CO_3^{2-} is known to increase solubility [3,4], this may explain the increased rate of recrystallisation in CHA-2 when compared to CHA-1.

This study was able to compare two synthetic samples at smaller temperature steps than has been used previously (Ivanova et al. used steps of either 25 °C or 50 °C). Ivanova et al. noted four 'plateaus' within

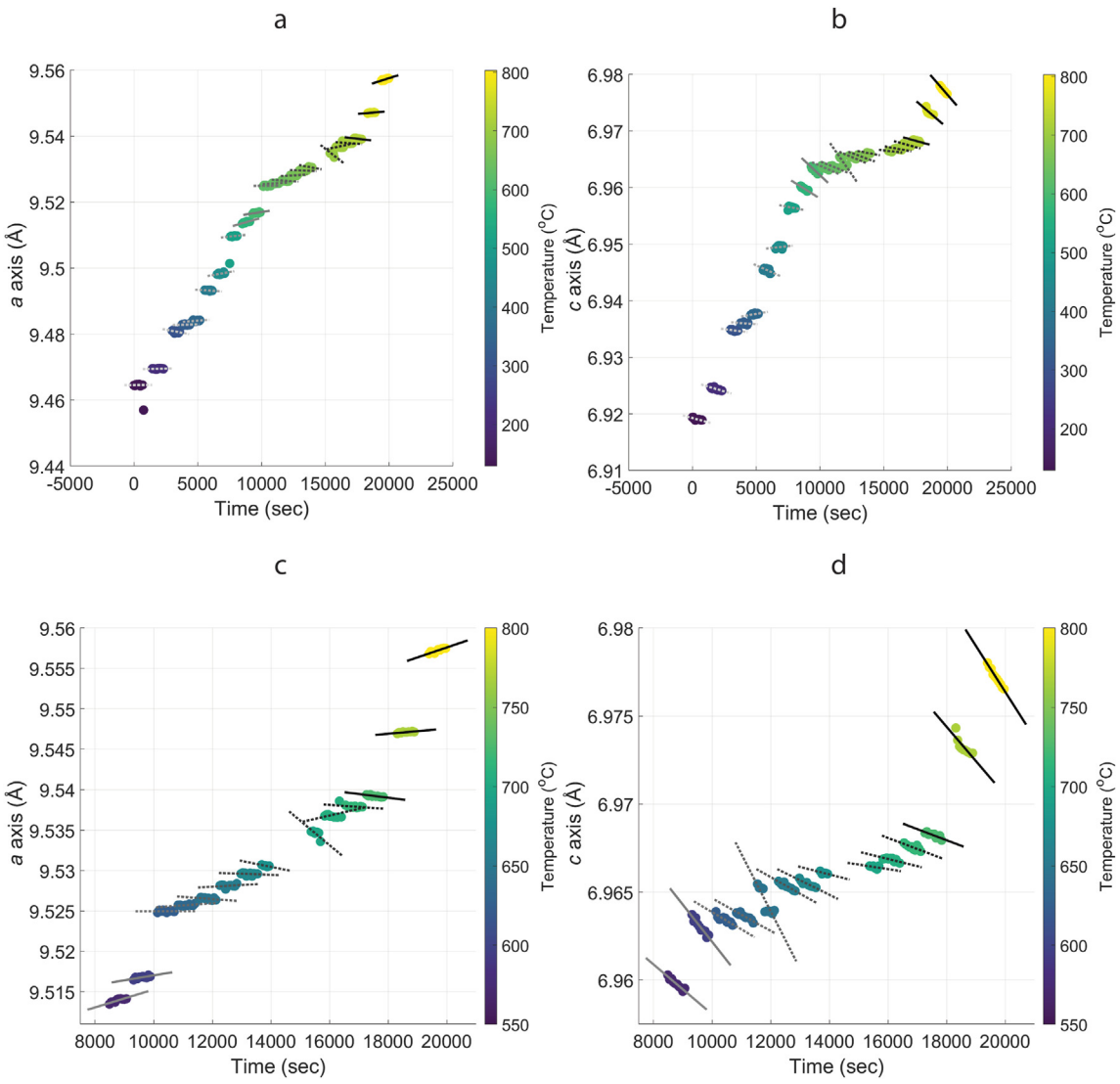

Fig. 6. Lattice parameters for dynamic measurements plotted against time of measurement since first measurement. *a)* and *b)* show *a* and *c* LPs respectively. *c)* and *d)* show *a* and *c* LPs respectively between 550 °C and 800 °C. For each temperature, a linear regression was performed, and is shown using either a solid line for a significant model ($p < 0.05$) or a dotted line for a model which is not significant ($p > 0.05$).

lattice parameters for a synthetic sample which was dynamically heated: 300 °C–350 °C and 400 °C–450 °C for *a* and 250 °C–300 °C and 350 °C–450 °C for *c*. These differences from 300 °C to 350 °C and 250 °C–300 °C are attributed to loss of two types of structural water. A similar 'plateau' is observed for both the synthetic samples within this study from 300 °C to 350 °C for both the *a* and *c* axis LPs. Further to this dehydration, Ivanova describes two periods of 'decarbonation' accompanied by changes in LPs from 400 °C to 450 °C and 600 °C–750 °C. While these are not observed within our study, significant changes are measured from 575 °C to 680 °C. This difference, a significant increase in *a* between 575 °C and 600 °C and a plateau in *c* from 575 °C to 620 °C, can be attributed to either an increase in A-type CO_3^{2-} or a decrease in B-type CO_3^{2-}. This is consistent with the results of Greenwood et al., where in human bone, the changes in both *a* and *c* started at the same temperature (580 °C) the change in *c* continued until 640 °C while the change in *a* discontinued around 620 °C.

Perhaps most interesting is the examination of LPs for each frame of CHA-2. From this analysis (particularly *c*) it is evident the changes observed between temperatures are not instantaneous, but rather are gradual over several minutes. As these changes are not seen to plateau during the 10 min dwell period, there is a possibility that these changes would continue past the point where temperature was changed in this study.

This is supported by the analysis of LPs over each temperature. While it is apparent that a great change occurs between 575 °C and 600 °C, seen from the increase in *a* and the lack of change in *c* (an effective decrease when considering the thermal expansion one would expect), more subtle changes are seen in the surrounding temperatures. This is indicated by the significant increase and decrease in *a* and *c* respectively at 550 °C and 575 °C, as well as a similar trend (though not significant) in the surrounding temperatures. It is proposed that a considerable decrease in B-type substituted CO_3^{2-} occurs between 550 °C and 600 °C, with a relatively small decrease in B-type substitution in the surrounding temperatures.

Additionally, significant relationships are seen in both *a* and *c* for 750 °C and 800 °C, indicating another process occurring, again slower than the time needed to increase the temperature and detectable beyond the thermal expansion seen. The significant increase in *a* and decrease in *c* is consistent with an increase in A-type CO_3^{2-}, seen in heat treated dental enamel when examined by FTIR [23], though no indication of this change was seen in biological samples when examined with XRD [20].

From examination of fractional coordinates, rigid body parameters

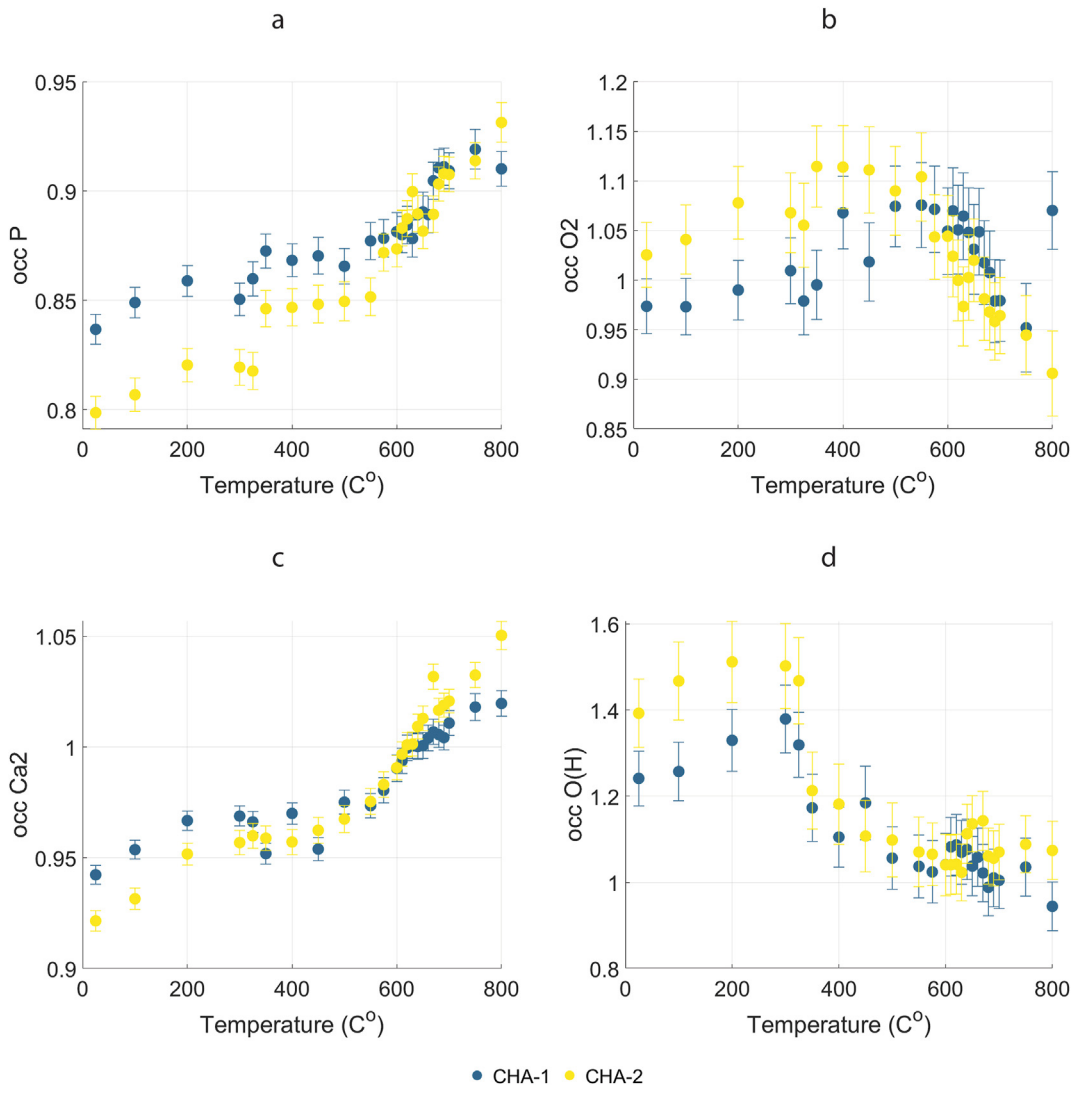

Fig. 7. Occupancies of atomic species correlated to temperature for both samples. Error bars represent estimated standard deviation.

and occupancy of atomic species, three distinct temperature ranges are apparent: 25 °C–350 °C, 350 °C–600 °C and 600 °C–800 °C, similar to those proposed by Ivanova et al. and Greenwood et al. [9,20]. Our data suggests that the lower temperature range encompasses both the reversible loss of adsorbed water and the irreversible loss of structural water, well described in literature [9,20–22,49]. The second range is structurally not well understood but is consistent with the loss of various substitutional ions (HPO_4^{2-}, Na^+, etc.) and the evacuation of B-type CO_3^{2-} [9,20]. The third range is commonly considered to include the loss of CO_3^{2-} and recrystallisation [18,20,22,50].

The majority of significant changes above 600 °C are consistent with a decrease in CO_3^{2-} substitution observed in stoichiometric samples measured at room temperature [39]. Ca1 *z*, Ca2 *x*, Ca2 *y*, O(H) *z* change consistently with a reduction in the amount of B-type CO_3^{2-}. A change is expected in OH *z* corresponding to 'ordering' of OH^- ions within the ion channel which occurs during the heating process. Studies which have previously examined HA after heat treatment (particularly biogenic HA where the OH^- absorption band in FTIR is often weak or absent in unheated bone) report an increase of the absorption bands near 3560 cm^{-1} and 630 cm^{-1} at temperatures of 300 °C or higher [16,23,51–53]. This research presents the first time the ion channel was able to be examined structurally during heating. We can see that the expected loss of lattice bound water [22,54] is accompanied by no change in the *z* fractional coordinate for the O(H), but a readily apparent contraction in the ion channel, through a decrease in Ca2 *x*.

Changes to the Ca2 occupancy follow that of P closely, potentially indicating that charge balancing of either PO_4^{3-} vacancy or CO_3^{2-} substitution may be primarily balanced by modification to the Ca2 site. Though this change cannot be fully elucidated without elemental analysis, it is likely due to loss of substitutions (presumably Na^+ due to the synthesis procedure) during recrystallisation. Although the Ca:P ratio appears variable, it decreases steadily towards 1.67 (the stoichiometric value) as temperature increases. This is consistent with the recrystallisation [20] where an increase in crystal size and order is concomitant with fewer vacancies and substitutions.

Most temperature factors of rigid bodies seem to be unaffected on a local scale by an increase in temperature, as would be expected. Of most interest is the variation of the *beqhi* parameters for component atoms of the rigid bodies, as previous studies on HA and other systems have shown similar or equivalent parameters (temperature factors *b* or isotropic displacement factors *B*) only increasing as temperature increases [19,55–57].

While increasing CO_3^{2-} concentration doesn't seem to affect local order (*beqlo*) it does affect intermediate order (*beqhi*), as expected from room temperature results. Each *beqhi* value is lower for CHA-1 than for CHA-2 until around 600 °C when recrystallisation begins. Average ordering of the ion channel (Ca2) seems to reach a maximum prior to recrystallisation. An increase in correlated motion (a decrease in *beqhi*) is

observed for the majority of atoms above the onset of recrystallisation. This is not as prominent for O1 and O3, as these atoms are shared between the PO_4^{3-} and the CO_3^{2-} when substituted in the C1 position.

Further consideration of the *beqhi* values of O(H) indicates that the OH^- group begins to become more ordered at high *r* at around 300 °C, and this order further increases with increasing temperature. This is consistent with the findings of Shi et al. [23], where the emergence of an OH out of plane bending vibration band (near 630 cm^{-1} [47,53]) was reported when dental enamel was heated to 300 °C. The precise mechanism which causes the OH^- absorption band to appear is not clear [52]. It is proposed the appearance or increase of these absorption bands corresponds to a loss of lattice-bound water and an ordering of the OH^- ion, seen here above 300 °C.

5. Conclusions

Significant changes are seen in local order of carbonated and stoichiometric HA, as would be expected from previous studies of local and average order of synthetic hydroxyapatites [9,28,37,58,59]. However, it should be noted that changes here are relatively quick, generally occurring between two adjacent temperatures where previous studies have seen much larger ranges in biogenically derived samples [20,23]. It is unclear whether these differences arise from differences in experimental conditions or differences in the material. The use of small box modelling showed great success, both at room temperature previously [39] and dynamic measurements here, though caution should still be observed for samples which are known to be anisotropic, as this method does not allow for any representation of crystallite anisotropy. Regardless, this method presents a new approach to measure the smallest dimension of HA crystallites. The consequence of a face-substituted CO_3^{2-} has been examined on a local scale, dynamically from 25 °C to 800 °C. Additionally, evidence has shown that CO_3^{2-} affects intermediate (and therefore likely average) order, but not local order. Dynamic studies have agreed with previous studies, both examining lattice parameters and crystallite size. This study has also seen an increase in A-type CO_3^{2-} at elevated temperatures, not seen before using diffraction. Furthermore, ordering of OH^- within the c-axis channel during heat treatment has agreed with static FTIR studies. Observing both the increase in A-type CO_3^{2-} and the ordering of OH dynamically is the first indication that these are not processes that occur during cooling, but that they occur during heating. Further understanding of synthetic HA, and the methods used to characterize the local order of this material can potentially be applied to biogenic material in the future, with implications for forensic, biomedical and clinical settings.

Funding sources

The work was partly supported by an Engineering & Physical Sciences Research Council grant (EP/T034238/1). This work was also partly supported by a Royal Society and Wolfson Foundation Fellowship (RSWF/R1/180012). This work was carried out with the support of the Diamond Light Source, instrument I15-1 (proposal cy24283).

CRediT authorship contribution statement

Emily L. Arnold: conceived the idea. conducted the experiment. analyzed the data and wrote the manuscript. **Sarah Gosling:** conducted the experiment. **Samantha K. Davies:** conducted the experiment. **Hannah L. Cross:** conducted the experiment. **Paul Evans:** reviewed the manuscript. **Dean S. Keeble:** conducted the experiment. **Charlene Greenwood:** conceived the idea. conducted the experiment. revised the manuscript. **Keith D. Rogers:** conceived the idea. revised the manuscript.

Declaration of competing interest

The authors declare that they have no known competing financial interests or personal relationships that could have appeared to influence the work reported in this paper.

Data availability

Data underlying this study can be accessed through the Cranfield University repository (CORD) at: 10.17862/cranfield.rd.19886560. Data are available under the terms of the [Creative Commons Attribution 4.0 International (CC BY 4.0)].

Acknowledgements

N. Stone of Exeter University is acknowledged for providing carbonate hydroxyapatite samples used for calibration. The work was partly supported by an Engineering & Physical Sciences Research Council grant (EP/T034238/1). This work was also partly supported by The Royal Society, and The Wolfson Foundation (RSWF/R1/180012). This work was carried out with the support of the Diamond Light Source, instrument I15-1 (proposal cy24283).

Appendix A. Supplementary data

Supplementary data to this article can be found online at https://doi.org/10.1016/j.jssc.2022.123474.

Abbreviations

ATR	attenuated total reflectance
CHA	carbonated hydroxyapatite;
FTIR	Fourier transform infrared spectroscopy
HA	hydroxyapatite;
PDF	pair distribution function
XRD	X-ray diffraction

References

[1] E. Bonucci, Bone mineralization, Front. Biosci. 17 (2012) 100–128, https://doi.org/10.2741/3918.
[2] S. von Euw, Y. Wang, G. Laurent, C. Drouet, F. Babonneau, N. Nassif, T. Azaïs, Bone mineral: new insights into its chemical composition, Sci. Rep. 9 (2019) 1–11, https://doi.org/10.1038/s41598-019-44620-6.
[3] B. Wopenka, J.D. Pasteris, A mineralogical perspective on the apatite in bone, Mater. Sci. Eng. C 25 (2005) 131–143, https://doi.org/10.1016/j.msec.2005.01.008.
[4] P. Grøn, M. Spinelli, O. Trautz, F. Brudevold, The effect of carbonate on the solubility of hydroxylapatite, Arch. Oral Biol. 8 (1963) 251–263, https://doi.org/10.1016/0003-9969(63)90016-5.
[5] R.Z. LeGeros, O.R. Trautz, Apatite crystallites: effects of carbonate on morphology, Science 155 (1967) 1409–1411, 1979.
[6] A.C. Deymier, A.K. Nair, B. Depalle, Z. Qin, K. Arcot, C. Drouet, C.H. Yoder, M.J. Buehler, S. Thomopoulos, G.M. Genin, J.D. Pasteris, Protein-free formation of bone-like apatite: new insights into the key role of carbonation, Biomaterials 127 (2017) 75–88, https://doi.org/10.1016/j.biomaterials.2017.02.029.
[7] C. Rey, C. Combes, C. Drouet, M.J. Glimcher, Bone mineral: update on chemical composition and structure, Osteoporos. Int. 20 (2009) 1013–1021, https://doi.org/10.1007/s00198-009-0860-y.
[8] R.M. Wilson, J.C. Elliott, S.E.P. Dowker, R.I. Smith, Rietveld structure refinement of precipitated carbonate apatite using neutron diffraction data, Biomaterials 25 (2004) 2205–2213, https://doi.org/10.1016/j.biomaterials.2003.08.057.
[9] T.I. Ivanova, O. v Frank-Kamenetskaya, A.B. Kol'tsov, V.L. Ugolkov, Crystal structure of calcium-deficient carbonated hydroxyapatite. Thermal decomposition, J. Solid State Chem. 160 (2001) 340–349, https://doi.org/10.1006/jssc.2000.9238.
[10] S. Beckett, K.D. Rogers, J.G. Clement, Inter-species variation in bone mineral behavior upon heating, J. Forensic Sci. 56 (2011) 571–579, https://doi.org/10.1111/j.1556-4029.2010.01690.x.
[11] S.T.D. Ellingham, T.J.U. Thompson, M. Islam, G. Taylor, Estimating temperature exposure of burnt bone - a methodological review, Sci. Justice 55 (2015) 181–188, https://doi.org/10.1016/j.scijus.2014.12.002.
[12] G. Piga, M.D. Baro, I.G. Escobal, D. Gonçalves, C. Makhoul, A. Amarante, A. Malgosa, S. Enzo, S. Garroni, A structural approach in the study of bones: fossil and burnt bones at nanosize scale, Appl. Phys. Mater. Sci. Process 122 (2016) 1–12, https://doi.org/10.1007/s00339-016-0562-1.
[13] P. Shipman, G. Foster, M. Schoeninger, Burnt bones and teeth: an experimental study of color, morphology, crystal structure and shrinkage, J. Archaeol. Sci. 11 (1984) 307–325, https://doi.org/10.1016/0305-4403(84)90013-X.

[14] F. Iqbal, H. Fatima, Coating of hydroxyapatite and substituted apatite on dental and orthopedic implants, in: A.S. Khan, A.A. Chaudhry (Eds.), Handbook of Ionic Substituted Hydroxyapatites, Elsevier, Oxford, 2020, pp. 327–354.

[15] C. Greenwood, K.D. Rogers, S. Beckett, J.G. Clement, Bone mineral crystallisation kinetics, J. Mater. Sci. Mater. Med. 23 (2012) 2055, https://doi.org/10.1007/s10856-012-4679-2. –2060.

[16] D. Gonçalves, A.R. Vassalo, A.P. Mamede, C. Makhoul, G. Piga, E. Cunha, M.P.M. Marques, L.A.E. Batista de Carvalho, Crystal clear: vibrational spectroscopy reveals intrabone, intraskeleton, and interskeleton variation in human bones, Am. J. Phys. Anthropol. 166 (2018) 296–312, https://doi.org/10.1002/ajpa.23430.

[17] M. Mckinnon, M. Henneberg, E. Simpson, D. Higgins, A comparison of crystal structure in fresh, burned and archaic bone - implications for forensic sampling, Forensic Sci. Int. 313 (2020), 110328, https://doi.org/10.1016/j.forsciint.2020.110328.

[18] S.M. Londoño-Restrepo, M. Herrera-Lara, L.R. Bernal-Alvarez, E.M. Rivera-Muñoz, M.E. Rodriguez-García, In-situ XRD study of the crystal size transition of hydroxyapatite from swine bone, Ceram. Int. 46 (2020) 24454–24461, https://doi.org/10.1016/j.ceramint.2020.06.230.

[19] A.T. Sänger, W.F. Kuhs, Structural disorder in hydroxyapatite, Z. für Kristallogr. - Cryst. Mater. 199 (1992) 123–148, https://doi.org/10.1524/zkri.1992.199.14.123.

[20] C. Greenwood, K.D. Rogers, S. Beckett, J.G. Clement, Initial observations of dynamically heated bone, Cryst. Res. Technol. 48 (2013) 1073–1082, https://doi.org/10.1002/crat.201300254.

[21] K. Tõnsuaadu, K.A. Gross, L. Pluduma, M. Veiderma, A review on the thermal stability of calcium apatites, J. Therm. Anal. Calorim. 110 (2012) 647–659, https://doi.org/10.1007/s10973-011-1877-y.

[22] R.Z. LeGeros, G. Bonel, R. Legros, Types of " H20 " in human enamel and in precipitated apatites preparation of human enamel samples X-ray diffraction analyses materials and methods preparation of synthetic apatites, Calcif. Tissue Res. 118 (1978) 111–118.

[23] J. Shi, A. Klocke, M. Zhang, U. Bismayer, Thermally-induced structural modification of dental enamel apatite: decomposition and transformation of carbonate groups, Eur. J. Mineral 17 (2005) 769–775, https://doi.org/10.1127/0935-1221/2005/0017-0769.

[24] I.R. Gibson, I. Rehman, S.M. Best, W. Bonfield, Characterization of the transformation from calcium-deficient apatite to β-tricalcium phosphate, J. Mater. Sci. Mater. Med. 11 (2000) 799–804, https://doi.org/10.1023/A:1008905613182.

[25] R.Z. LeGeros, O.R. Trautz, E. Klein, J.P. LeGeros, Two types of carbonate substitution in the apatite structure, Experientia 25 (1969) 5–7, https://doi.org/10.1007/BF01903856.

[26] R.Z. LeGeros, Effect of carbonate on the lattice parameters of apatite, Nature 206 (1965) 403–404, https://doi.org/10.1038/206403a0.

[27] H. Madupalli, B. Pavan, M.M.J. Tecklenburg, Carbonate substitution in the mineral component of bone: discriminating the structural changes, simultaneously imposed by carbonate in A and B sites of apatite, J. Solid State Chem. 255 (2017) 27–35, https://doi.org/10.1016/j.jssc.2017.07.025.

[28] M.E. Fleet, X. Liu, Location of type B carbonate ion in type A-B carbonate apatite synthesized at high pressure, J. Solid State Chem. 177 (2004) 3174–3182, https://doi.org/10.1016/j.jssc.2004.04.002.

[29] M.E. Fleet, X. Liu, Type A-B carbonate chlorapatite synthesized at high pressure, J. Solid State Chem. 181 (2008) 2494–2500, https://doi.org/10.1016/j.jssc.2008.06.016.

[30] P.W. Brown, B. Constantz, Hydroxyapatite and Related Materials, CRC Press, 1994.

[31] J.C. Elliott, Calcium phosphate biominerals, in: Phosphates: Geochemical, Geobiological and Materials Importance, 2002, pp. 427–454, https://doi.org/10.2138/rmg.2002.48.11.

[32] C. Rey, B. Collins, T. Goehl, I.R. Dickson, M.J. Glimcher, The carbonate environment in bone mineral: a resolution-enhanced fourier transform infrared spectroscopy study, Calcif. Tissue Int. 45 (1989) 157–164, https://doi.org/10.1007/BF02556059.

[33] E.P. Paschalis, R. Mendelsohn, A.L. Boskey, Infrared assessment of bone quality: a review, Clin. Orthop. Relat. Res. 469 (2011) 2170–2178, https://doi.org/10.1007/s11999-010-1751-4.

[34] L.M. Miller, G.D. Smith, G.L. Carr, Synchrotron-based biological microspectroscopy: from the mid-infrared through the far-infrared regimes, J. Biol. Phys. 29 (2003) 219–230, https://doi.org/10.1023/A:1024401027599.

[35] C. Benetti, S.G. Kazarain, M.A. v Alves, A. Blay, L. Correa, D.M. Zezell, Attenuated total reflection Fourier transform infrared (ATR-FTIR) spectroscopic analysis of regenerated bone, Photon. Therapeut. Diagn. X 8926 (2014), 892641, https://doi.org/10.1117/12.2039915.

[36] V. v Chasov, I.S. Raginov, S.N. Medvedeva, I. Safin, A.A. Rizvanov, Fourier transform infrared spectroscopy analysis of human osteosarcoma bone tissue, Bionanoscience 8 (2018) 481–483, https://doi.org/10.1007/s12668-018-0500-0.

[37] E.L. Arnold, D.S. Keeble, C. Greenwood, K.D. Rogers, New insights into the application of pair distribution function studies to biogenic and synthetic hydroxyapatites, Sci. Rep. 10 (2020) 1–11, https://doi.org/10.1038/s41598-020-73200-2.

[38] J.C. Merry, I.R. Gibson, S.M. Best, W. Bonfield, Synthesis and characterization of carbonate hydroxyapatite, J. Mater. Sci. Mater. Med. 9 (1998) 779–783, https://doi.org/10.1023/A:1008975507498.

[39] E.L. Arnold, D.S. Keeble, J.P.O. Evans, C. Greenwood, K.D. Rogers, Investigating pair distribution function use in analysis of nanocrystalline hydroxyapatite and carbonate-substituted hydroxyapatite, Acta Crystallogr. C: Struct. Chem. (2022), https://doi.org/10.1107/S2053229622003400.

[40] M. Basham, J. Filik, M.T. Wharmby, P.C.Y. Chang, B. el Kassaby, M. Gerring, J. Aishima, K. Levik, B.C.A. Pulford, I. Sikharulidze, D. Sneddon, M. Webber, S.S. Dhesi, F. Maccherozzi, O. Svensson, S. Brockhauser, G. Náray, A.W. Ashton, A.W. Ashton, G. Naray, A.W. Ashton, G. Náray, A.W. Ashton, A.W. Ashton, G. Naray, A.W. Ashton, Data analysis WorkbeNch (DAWN), J. Synchrotron Radiat. 22 (2015) 853–858, https://doi.org/10.1107/S1600577515002283.

[41] A.K. Soper, E.R. Barney, Extracting the pair distribution function from white-beam X-ray total scattering data, J. Appl. Crystallogr. 44 (2011) 714–726, https://doi.org/10.1107/S0021889811021455.

[42] A.A. Coelho, P.A. Chater, A. Kern, Fast synthesis and refinement of the atomic pair distribution function, J. Appl. Crystallogr. 48 (2015) 869–875, https://doi.org/10.1107/S1600576715007487.

[43] A.A. Coelho, TOPAS and TOPAS-Academic: an optimization program integrating computer algebra and crystallographic objects written in C++: an, J. Appl. Crystallogr. 51 (2018) 210–218, https://doi.org/10.1107/S1600576718000183.

[44] K. Kodama, S. Iikubo, T. Taguchi, S. Shamoto, Finite size effects of nanoparticles on the atomic pair distribution functions, Acta Crystallogr. A A62 (2006) 444–453, https://doi.org/10.1107/S0108767306034635.

[45] M.I. Kay, R.A. Young, A.S. Posner, Crystal structure of hydroxyapatite, Nature 204 (1964) 1050–1052, https://doi.org/10.1038/2041050a0.

[46] P.A. Chater, topas. https://github.com/pachater/topas, 2017.

[47] G. Socrates, Infrared and Raman Characteristic Group Frequencies, John Wiley & Sons Ltd, Chichester, 2001.

[48] K.A. Hing, J.C. Merry, I.R. Gibson, L. Di-Silvio, S.M. Best, W. Bonfield, Effect of Carbonate Content on the Response of Human Osteoblast-like Cells to Carbonate Substituted Hydroxyapatite, Bioceramics, 1999, pp. 195–198.

[49] C.J. Liao, F.H. Lin, K.S. Chen, J.S. Sun, Thermal decomposition and reconstitution of hydroxyapatite in air atmosphere, Biomaterials 20 (1999) 1807–1813, https://doi.org/10.1016/S0142-9612(99)00076-9.

[50] K.D. Rogers, P. Daniels, An X-ray diffraction study of the effects of heat treatment on bone mineral microstructure, Biomaterials 23 (2002) 2577–2585, https://doi.org/10.1016/S0142-9612(01)00395-7.

[51] N. Bano, S.S. Jikan, H. Basri, S. Adzila, D.M. Zago, XRD and FTIR study of A&B type carbonated hydroxyapatite extracted from bovine bone, AIP Conf. Proc. (2019) 2068, https://doi.org/10.1063/1.5089399.

[52] C. Rey, J.L. Miquel, L. Facchini, A.P. Legrand, M.J. Glimcher, Hydroxyl groups in bone mineral, Bone 16 (1995) 583–586, https://doi.org/10.1016/8756-3282(95)00101-I.

[53] T.J.U. Thompson, M. Islam, M. Bonniere, A new statistical approach for determining the crystallinity of heat-altered bone mineral from FTIR spectra, J. Archaeol. Sci. 40 (2013) 416–422, https://doi.org/10.1016/j.jas.2012.07.008.

[54] L.D. Mkukuma, C.T. Imrie, J.M.S. Skakle, D.W.L. Hukins, R.M. Aspden, Thermal stability and structure of cancellous bone mineral from the femoral head of patients with osteoarthritis or osteoporosis, Ann. Rheum. Dis. 64 (2005) 222–225, https://doi.org/10.1136/ard.2004.021329.

[55] K. Yamanaka, M. Yamagami, T. Takamuku, T. Yamaguchi, H. Wakita, X-Ray diffraction study on aqueous lithium chloride solution in the temperature range 138-373 K. https://pubs.acs.org/sharingguidelines, 1993.

[56] E.S. Božin, V. Petkov, P.W. Barnes, P.M. Woodward, T. Vogt, S.D. Mahanti, S.J.L. Billinge, Temperature dependent total scattering structural study of CaCu 3Ti4O12, J. Phys. Condens. Matter (2004), https://doi.org/10.1088/0953-8984/16/44/007.

[57] A.H. Clark, N. Acerbi, P.A. Chater, S. Hayama, P. Collier, T.I. Hyde, G. Sankar, Temperature reversible synergistic formation of cerium oxyhydride and Au hydride: a combined XAS and XPDF study, Phys. Chem. Chem. Phys. 22 (2020) 18882–18890, https://doi.org/10.1039/d0cp00455c.

[58] M.E. Marisa, S. Zhou, B.C. Melot, G.F. Peaslee, J.R. Neilson, Paracrystalline disorder from phosphate ion orientation and substitution in synthetic bone mineral, Inorg. Chem. 55 (2016) 12290–12298, https://doi.org/10.1021/acs.inorgchem.6b02025.

[59] M.E. Fleet, X. Liu, Local structure of channel ions in carbonate apatite, Biomaterials 26 (2005) 7548–7554, https://doi.org/10.1016/j.biomaterials.2005.05.025.